

**Research Highlights (Required)**

To create your highlights, please type the highlights against each `\item` command.

It should be short collection of bullet points that convey the core findings of the article. It should include 3 to 5 bullet points (maximum 85 characters, including spaces, per bullet point.)

- Propose a new hyperspectral subpixel target detection method called MSDH.
- Extend the classical MSD to allow for unequal noise intensities over different bands.
- Demonstrate the superiority of MSDH on real hyperspectral data.



## MSDH: Matched Subspace Detector with Heterogeneous Noise

Xiaochen Yang<sup>a</sup>, Lefei Zhang<sup>b</sup>, Lianru Gao<sup>c</sup>, Jing-Hao Xue<sup>a,\*\*</sup>

<sup>a</sup>Department of Statistical Science, University College London, London WC1E 6BT, U.K.

<sup>b</sup>School of Computer Science, Wuhan University, Wuhan 430072, China

<sup>c</sup>Key Laboratory of Digital Earth Science, Institute of Remote Sensing and Digital Earth, Chinese Academy of Sciences, Beijing 100094, China

Article history:

**Keywords:** Hyperspectral imaging, matched subspace detector (MSD), target detection, heterogeneous noise

### ABSTRACT

The matched subspace detector (MSD) is a classical subspace-based method for hyperspectral subpixel target detection. However, the model assumes that noise has the same variance over different bands, which is usually unrealistic in practice. In this letter, we relax the equal variance assumption and propose a matched subspace detector with heterogeneous noise (MSDH). In essence, the noise variances are different for different bands and they can be estimated by using iteratively reweighted least squares methods. Experiments on two benchmark real hyperspectral datasets demonstrate the superiority of MSDH over MSD for subpixel target detection.

© 2019 Elsevier Ltd. All rights reserved.

### 1. Introduction

Hyperspectral imaging in remote sensing is a technology that collects the light intensity over a large number of narrow spectral bands for each pixel in the image of a scene. For any given material, the amount of radiation that is reflected, absorbed or emitted varies with wavelength [1]. Therefore, the spectral characteristic of hyperspectral images (HSIs) offers potential for precise identification of materials in a scene. Target detection in hyperspectral images aims to find the location of interested targets at the pixel level by exploiting their spectral information, which has numerous applications in various fields. When the target size is smaller than the ground sampling distance, a pixel containing target will be partially occupied by background (non-target) materials; target detection in this scenario is termed subpixel target detection.

Classical approaches to HSI target detection can be categorized into subspace-based models and statistical models [1]. In subspace-based models [2, 3], each spectrum is assumed to lie in a low-dimensional subspace and represented as a linear combination of subspace bases. In statistical models [4, 5], each spectrum is assumed to follow specific probability distributions. In both approaches, each pixel in the scene is identified as target or background via hypothesis testing. Based on these work,

hybrid approaches have been proposed to take advantage of both types of methods [6, 7], as well as further development within each category, such as [8–11] for subspace-based models and [12] for statistical models. To avoid estimating subspaces and distribution parameters, a series of sparse representation (SR)-based methods have been proposed, which assume that a signal can be sparsely represented by a small number of training samples [13, 14], and they have been combined with classical methods [15]. More recently, methods in machine learning have been adopted for specific purposes, such as metric learning for maximising the separability between target and background spectra [16–18], multi-instance learning for learning a target spectrum [19] and multi-task learning for removing spectral redundancy [20].

In classical subspace-based methods, a pixel is modelled as a linear combination of subspace bases with the additive Gaussian white noise of equal variances over different spectral bands. This equal-variance assumption, however, is unrealistic in practice, as noise is of unequal intensities over different bands; the unequal intensity phenomenon is often caused by thermal noise and quantization noise [21]; and the violation of the assumption will impair the effectiveness of subspace-based methods. To address this issue, one solution is to apply denoising prior to target detection. In most denoising algorithms, however, there is a parameter to trade off between data fidelity and regularization on the denoised image, and determining the optimal value of this parameter is a challenging task. Another

\*\*Corresponding author: Tel.: +44-207-679-1863  
e-mail: [jinghao.xue@ucl.ac.uk](mailto:jinghao.xue@ucl.ac.uk) (Jing-Hao Xue)

solution is to estimate the noise intensity of each band [22]. However, as most classical methods produce the noise estimation for the entire HSI, rather than for each pixel, its effectiveness may be limited.

In this letter, we propose a new subpixel target detection method called matched subspace detector with heterogeneous noise (MSDH) to take into account of unequal noise intensities over different bands. Our MSDH method consists of three steps. Firstly, we revise the covariance matrix of the Gaussian noise, from an identity matrix in the classical matched subspace method (MSD) to a diagonal matrix with unequal diagonal elements. These diagonal elements characterize the noise intensities over different spectral bands. Secondly, we derive the new target detector based on the generalized likelihood ratio test. Thirdly, we adapt an iterative reweighted least squares algorithm to estimate unknown parameters in our model including those on noise intensities. The effectiveness of MSDH is demonstrated via empirical studies on two HSI datasets in a real setting, as well as in a simulated setting where heterogeneous noise is added to the original datasets.

## 2. The matched subspace detector (MSD)

The matched subspace detector (MSD) is a classical subspace-based method; it assumes that a pure background spectrum or a pure target spectrum can be represented as a linear combination of bases from the background subspace or from the target subspace, respectively. For subpixel target detection, deciding whether a pixel contains the target is equivalent to determining whether it lies in the background subspace or in the target-background joint subspace; here, the joint subspace is used since subpixel targets occupy only part of the pixel and the remaining area is filled by background material. More formally, the target detection problem for an HSI pixel  $\mathbf{x} \in \mathbb{R}^L$  is a competition between the following two hypotheses:

$$\begin{aligned} H_0 : \mathbf{x} &= \mathbf{S}_b \boldsymbol{\alpha}_{b,0} + \mathbf{w}_b && \text{(target absent),} \\ H_1 : \mathbf{x} &= \mathbf{S}_t \boldsymbol{\alpha}_t + \mathbf{S}_b \boldsymbol{\alpha}_{b,1} + \mathbf{w}_t && \text{(target present),} \end{aligned} \quad (1)$$

where  $\mathbf{S}_b$  is an  $L \times r_b$  matrix representing the background subspace,  $\mathbf{S}_t$  is an  $L \times r_t$  matrix representing the target subspace;  $\mathbf{w}_b \sim \mathcal{N}(\mathbf{0}, \sigma_{wb}^2 \mathbf{I})$  and  $\mathbf{w}_t \sim \mathcal{N}(\mathbf{0}, \sigma_{wt}^2 \mathbf{I})$  represent the Gaussian white noise vectors;  $L$  denotes the number of spectral bands;  $r_b$  is the number of bases in the background subspace; and  $r_t$  represents the number of bases in the target subspace. Moreover,  $r_b$  and  $r_t$  are constrained to be smaller than  $L$ . We introduce notations  $\mathbf{S}_{tb} = [\mathbf{S}_t, \mathbf{S}_b]$  and  $\boldsymbol{\alpha}_{tb} = [\boldsymbol{\alpha}_t, \boldsymbol{\alpha}_{b,1}]$  to denote the concatenation of subspace matrices and that of coefficient vectors, respectively, for later use.

The background subspace is generally unknown and may be constructed from the training data of background. [23] suggested to diagonalize the covariance matrix and select the dominant eigenvectors as the bases of the background subspace. [24] used the first few significant left-singular vectors of the data matrix. The target subspace is either specified by the user or constructed from the training target spectra in a way similar to that for the background.

The coefficient vectors  $\boldsymbol{\alpha}_{b,0}$  and  $\boldsymbol{\alpha}_{tb}$  and the variances  $\sigma_{wb}^2$  and  $\sigma_{wt}^2$  are unknown and can be replaced by their maximum likelihood estimators (MLE). As an example, here we estimate the parameters under  $H_0$ . The same method can be applied to parameter estimation under  $H_1$ . The MLEs are given as

$$\begin{aligned} \hat{\boldsymbol{\alpha}}_{b,0} &= (\mathbf{S}_b^T \mathbf{S}_b)^{-1} \mathbf{S}_b^T \mathbf{x}, \\ \hat{\sigma}_{wb}^2 &= \frac{1}{L} (\mathbf{x} - \mathbf{S}_b \hat{\boldsymbol{\alpha}}_{b,0})^T (\mathbf{x} - \mathbf{S}_b \hat{\boldsymbol{\alpha}}_{b,0}) = \frac{1}{L} \text{SSE}(\hat{\boldsymbol{\alpha}}_{b,0}), \end{aligned} \quad (2)$$

where SSE stands for the sum of squared prediction errors.

The decision on the existence of targets in  $\mathbf{x}$  is based on the generalized likelihood ratio (GLR): Let  $\mathcal{L}$  denote the likelihood function, then we have

$$\begin{aligned} \text{GLR}(\mathbf{x}) &= \frac{\mathcal{L}(\hat{\boldsymbol{\alpha}}_{tb}, \hat{\sigma}_{wt}^2; \mathbf{x})}{\mathcal{L}(\hat{\boldsymbol{\alpha}}_{b,0}, \hat{\sigma}_{wb}^2; \mathbf{x})} = \frac{(2\pi \frac{\text{SSE}(\hat{\boldsymbol{\alpha}}_{tb})}{L})^{-L/2} \exp(-\frac{L}{2})}{(2\pi \frac{\text{SSE}(\hat{\boldsymbol{\alpha}}_{b,0})}{L})^{-L/2} \exp(-\frac{L}{2})} \\ &= \left[ \frac{\text{SSE}(\hat{\boldsymbol{\alpha}}_{b,0})}{\text{SSE}(\hat{\boldsymbol{\alpha}}_{tb})} \right]^{L/2} = \left[ \frac{\mathbf{x}^T \mathbf{P}_b^\perp \mathbf{x}}{\mathbf{x}^T \mathbf{P}_{tb}^\perp \mathbf{x}} \right]^{L/2}, \end{aligned} \quad (3)$$

where  $\mathbf{P}_b = \mathbf{S}_b (\mathbf{S}_b^T \mathbf{S}_b)^{-1} \mathbf{S}_b^T$  is the orthogonal projection onto the column space of the background matrix  $\mathbf{S}_b$ , and  $\mathbf{P}_b^\perp = \mathbf{I} - \mathbf{P}_b$  is the orthogonal complement; similarly  $\mathbf{P}_{tb} = \mathbf{S}_{tb} (\mathbf{S}_{tb}^T \mathbf{S}_{tb})^{-1} \mathbf{S}_{tb}^T$  is the orthogonal projection onto the column space of the joint target and background matrix  $\mathbf{S}_{tb}$ , and  $\mathbf{P}_{tb}^\perp = \mathbf{I} - \mathbf{P}_{tb}$  is the orthogonal complement. Applying a monotone transformation, the MSD becomes

$$D_{\text{MSD}} = [\text{GLR}(\mathbf{x})^{2/L} - 1] = \frac{\mathbf{x}^T \mathbf{P}_b^\perp \mathbf{x} - \mathbf{x}^T \mathbf{P}_{tb}^\perp \mathbf{x}}{\mathbf{x}^T \mathbf{P}_{tb}^\perp \mathbf{x}} \underset{H_0}{\overset{H_1}{\geq}} \eta, \quad (4)$$

where  $\eta$  is the detection threshold. A pixel is labelled as target if  $D_{\text{MSD}}$  is larger than  $\eta$  and as background otherwise.

## 3. The matched subspace detector with heterogeneous noise (MSDH)

Rather than assuming equal noise variances over different bands, it is desirable to extend to unequal variances in order to characterise more noise types. The new assumption demands an iterative estimation of unknown parameters and results in a new detection statistic. The differences between MSD and MSDH are summarised in Table 1.

### 3.1. Formulation of MSDH

In order to model the heterogeneous noise, we relax the noise assumption of the MSD from white noise to a multivariate Gaussian noise whose covariance matrix is represented by a diagonal matrix with unequal diagonal elements.

The binary hypothesis for MSDH is as follows:

$$\begin{aligned} H_0 : \mathbf{x} &= \mathbf{S}_b \boldsymbol{\alpha}_{b,0} + \mathbf{w}_b && \text{(target absent),} \\ H_1 : \mathbf{x} &= \mathbf{S}_t \boldsymbol{\alpha}_t + \mathbf{S}_b \boldsymbol{\alpha}_{b,1} + \mathbf{w}_t && \text{(target present),} \end{aligned} \quad (5)$$

where  $\mathbf{w}_b \sim \mathcal{N}(\mathbf{0}, \mathbf{V}_b)$  and  $\mathbf{w}_t \sim \mathcal{N}(\mathbf{0}, \mathbf{V}_t)$ , in which  $\mathbf{V}_b$  and  $\mathbf{V}_t$  are diagonal covariance matrices.

As with the MSD, we estimate the coefficient vectors and the covariance matrix via MLE. The derivation for a background

	MSD	MSDH
Assumption on the noise term	Equal variances over spectral bands (identity covariance matrix)	Unequal variances over spectral bands (diagonal covariance matrix)
Parameter estimation ( $\alpha, \sigma^2/V$ )	Estimated in one step according to Eq. (2)	Estimated iteratively using IRLS (Sec. 3.2)
Detection statistic	Eq. (4)	Eq. (9)

Table 1: Differences between MSD and MSDH.

pixel is given below; the same procedure applies to a target pixel. The likelihood function is given by

$$\mathcal{L}(\alpha_{b,0}, \mathbf{V}_b; \mathbf{x}) = \frac{1}{\sqrt{(2\pi)^L \det(\mathbf{V}_b)}} e^{-\frac{1}{2}(\mathbf{x} - \mathbf{S}_b \alpha_{b,0})^T \mathbf{V}_b^{-1} (\mathbf{x} - \mathbf{S}_b \alpha_{b,0})}, \quad (6)$$

where  $\det(\mathbf{V}_b)$  denotes the determinant of  $\mathbf{V}_b$ . Taking the logarithmic transformation of the likelihood function, differentiating with respect to  $\alpha$  and  $\mathbf{V}$ , and setting them to zero give the estimators as follows:

$$\begin{aligned} \hat{\alpha}_{b,0} &= (\mathbf{S}_b^T \hat{\mathbf{V}}_b^{-1} \mathbf{S}_b)^{-1} \mathbf{S}_b^T \hat{\mathbf{V}}_b^{-1} \mathbf{x}, \\ \hat{\mathbf{V}}_b &= \text{diag}((x_1 - \mathbf{S}_{b,1} \hat{\alpha}_{b,0})^2, \dots, (x_L - \mathbf{S}_{b,L} \hat{\alpha}_{b,0})^2), \end{aligned} \quad (7)$$

where  $x_i$  is the  $i$ th element of  $\mathbf{x}$  and  $\mathbf{S}_{b,i}$  is the  $i$ th row of  $\mathbf{S}_b$ .

Then, we can derive the MSDH based on the GLR test:

$$\text{GLR}(x) = \left( \frac{\det(\hat{\mathbf{V}}_b)}{\det(\hat{\mathbf{V}}_t)} \right)^{\frac{1}{2}}. \quad (8)$$

For numerical stability, we take a logarithmic transformation of (8) and the MSDH is given by

$$D_{\text{MSDH}} = \sum_{i=1}^L \ln |x_i - \mathbf{S}_{b,i} \hat{\alpha}_{b,0}| - \sum_{i=1}^L \ln |x_i - \mathbf{S}_{t,i} \hat{\alpha}_{t,0}| \stackrel{H_1}{\geq} \eta. \quad (9)$$

### 3.2. Parameter estimation

The MLEs  $\hat{\alpha}$  and  $\hat{\mathbf{V}}$  in (7), with subscripts omitted for simplicity, depend on each other and therefore we need to update them in an iterative way. In this letter, we adapt an iteratively reweighted least squares (IRLS) algorithm [25].

Maximising the log-likelihood function with respect to  $\alpha$  is equivalent to minimising  $(\mathbf{x} - \mathbf{S}\alpha)^T \mathbf{V}^{-1} (\mathbf{x} - \mathbf{S}\alpha)$ , which can be written as a weighted least squares problem

$$\mathbf{x} = \mathbf{S}\alpha + \epsilon, \quad (10)$$

where  $\epsilon \sim \mathcal{N}(\mathbf{0}, \mathbf{V} = \text{diag}(v_1, \dots, v_L))$ , with  $w_i = 1/v_i$  as the weight of the  $i$ th band. Since a covariance matrix is positive semi-definite, we can always find a matrix  $\mathbf{K}$  such that  $\mathbf{K}\mathbf{K}^T = \mathbf{V}$ . By defining  $\tilde{\mathbf{x}} = \mathbf{K}^{-1}\mathbf{x}$ ,  $\tilde{\mathbf{S}} = \mathbf{K}^{-1}\mathbf{S}$ , and  $\tilde{\epsilon} = \mathbf{K}^{-1}\epsilon$ , (10) can be transformed into a least squares estimation (LSE) problem

$$\tilde{\mathbf{x}} = \tilde{\mathbf{S}}\alpha + \tilde{\epsilon}, \quad (11)$$

where  $\tilde{\epsilon} \sim \mathcal{N}(\mathbf{0}, \mathbf{I})$ .

The IRLS algorithm alternates between estimating the regression model of (11) and estimating the weight matrix  $\mathbf{W} = \text{diag}(w_1, \dots, w_L)$  (equivalently the covariance matrix  $\mathbf{V}$ ), as explained in the steps below:

1. Start with  $w_i = 1$  for all  $i$ ;
2. Use LSE to estimate  $\alpha$  in Eq. (11);
3. Calculate the residuals  $\hat{\epsilon} = \mathbf{x} - \hat{\mathbf{x}}$  in Eq. (10) and predict the weights  $w_1, \dots, w_L$ ;
4. Iterate between steps 2 and 3 until the change in the coefficient vector  $\alpha$  between steps is less than a predefined threshold, or until the number of iterations exceeds a predefined value.

In step 3, the weights can be calculated directly from the residuals as  $1/w_i = v_i = \hat{\epsilon}_i^2$  [26]. Alternatively, it can be predicted based on  $\hat{\epsilon}_i^2$  or  $\log(\hat{\epsilon}_i^2)$ , by using parametric models [27] or non-parametric methods [28]. In this letter, we adopt the former strategy [26]. To avoid that  $\hat{\epsilon}_i = 0$  in rare occasions leading to undefined  $w_i$ , we add a small constant  $c = 10^{-15}$  to all  $\hat{\epsilon}_i^2$ .

The computational cost of MSDH is  $MN$  times that of MSD, where  $M$  is the number of iterations used in the IRLS algorithm and  $N$  is the total number of pixels to be tested. To reduce the computational time, we only update the parameters once, i.e.  $M = 1$ . Experiments in Sec. 4 show that updating parameters once is sufficient for improving MSD. Moreover, we could reduce the number of testing pixels by adding a pre-screening step. Firstly, we select  $p$  percent ( $p < 100$ ) of the total  $N$  pixels that have the largest test statistics from MSD. Pixels that are not selected will be labelled as background. Secondly, we apply MSDH to the selected  $Np$  pixels. In this way, the computational cost is shrunk from  $N$  to  $Np$ . If  $p$  is large, the reduced computational cost is small; if  $p$  is too small, the pixel that contains the target may not get selected in the first step and consequently the target detection performance will deteriorate. In this letter, we set  $p = 10\%$ ; this choice is examined in Sec. 4.

## 4. Experiments

We compare MSDH against MSD and some classical target detection methods on two public HSI datasets for subpixel target detection. The first one is the HyMap dataset, a benchmark dataset for hyperspectral target detection [29–31]. The second dataset is the MUUFL dataset, which has been studied for image fusion [32], multi-instance learning [19], and hyperspectral unmixing [33, 34]. Two datasets differ by the number of samples available per target, and consequently we will use different measures to evaluate the performance of target detection methods, as suggested in [29] and [19].

### 4.1. The HyMap dataset

#### 4.1.1. Data description

The HyMap dataset was collected by the Rochester Institute of Technology in July 2006 over Cooke City, MT, USA [35].

The image has a spatial size of  $280 \times 800$  with a resolution of 3m and 126 spectral bands ranging from 450 to 2500 nm. Radiance and reflectance images are both provided and the reflectance image is used in this study.

The dataset includes seven targets, four of them are fabric panels (F1, F2, F3, F4) and the other three are vehicles (V1, V2, V3). While targets F1 and F2 have sizes of  $3\text{m} \times 3\text{m}$  that are same as the ground sampling distance, it is less likely that the target location exactly matches the collected pixel; therefore, we will still treat them as subpixel targets. Targets F3 and F4 come in two sizes ( $2\text{m} \times 2\text{m}$  for F3a and F4a, and  $1\text{m} \times 1\text{m}$  for F3b and F4b) and we will detect them separately.

#### 4.1.2. Experimental settings

As all targets locate in the central region of the HyMap image, we crop a sub-image of size  $100 \times 300$  in this experiment [9, 30, 36]. The cropped image and the ground-truth location of targets are shown in Fig. 1.

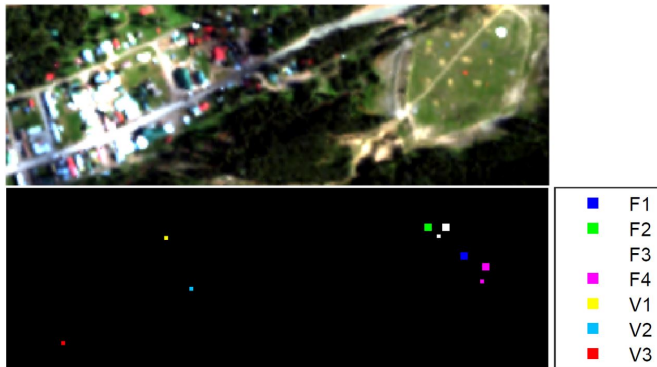


Fig. 1: Upper: The HyMap sub-image cropped from pixels (101:200, 251:550). Lower: Ground-truth locations of seven targets are marked in different colors; background pixels are in black.

The target location for F1, F2, F3a or F4a consists of 9 pixels, 1 pixel marked as ‘Full’ and 8 pixels marked as ‘Sub’ in the ROI files provided in [35]; the target location for F3b, F4b, V1, V2 or V3 consists of 1 pixel, marked as ‘Sub’. Information on guard pixels is available for all targets and these pixels do not count into target nor false alarms [37]. Moreover, at each time, only one target is to be detected and the other targets are considered as background pixels. The threshold in each hypothesis testing is selected as the largest value such that the target could be correctly identified. The evaluation criterion is the false alarm rate (FAR), which equals to the number of non-target pixels having a higher value of test statistic than the threshold, divided by the total number of pixels in the image, i.e. 30,000 in our study. A smaller value of FAR suggests a better detection performance.

To evaluate the effectiveness of MSDH, we compare it with some classical and widely used target detection methods, including a full-pixel target detection method, namely CEM [38], two statistical methods, namely AMF [4] and signed ACE (sACE) [39], and two subspace-based methods, namely OSP [2] and MSD [3]. Moreover, we perform noise estimation prior to MSD using three classical methods, namely local

means and local standard deviations (LMLSD) [40], residual-based noise estimation (RBNE) [41] and spectral and spatial de-correlation (SSDC) [42], which make use of spatial, spectral, and spatial and spectral information, respectively; the resultant methods are termed MSD+L, MSD+R and MSD+S. For CEM, AMF and sACE, the test statistic can be calculated based on the formula once the target spectrum is given. For MSD, MSDH and OSP, we need to construct background and target subspaces. The background subspace is constructed by using eigen-decomposition as suggested in [23]. The mean spectrum is subtracted from all pixels in the sub-image, eigen-decomposition is performed on the covariance matrix, and eigenvectors for the largest few eigenvalues form the background subspace. The number of eigenvectors in the background subspace, denoted as  $r_b$ , is selected from the range of [1, 124]. The target subspace is constructed from the single library spectrum by subtracting the background mean spectrum and normalizing to a unit length with respect to  $l_2$  norm.

For LMLSD and SSDC, the block sizes are set to  $4 \times 4$  and  $6 \times 6$  and the number of bins is set to 150 as suggested in [40] and [22]. After estimating the noise covariance matrix, we calculate the parameters with (7) and adopt the GLR as the detection statistic. Table 2 lists the optimal value of  $r_b$  used in subspace-based methods for each target.

Table 2: Parameter  $r_b$  in OSP, MSD and MSDH for the HyMap dataset.

	F1	F2	F3a	F3b	F4a	F4b	V1	V2	V3
OSP	27	26	20	88	51	45	10	4	67
MSD	25	21	11	10	51	42	10	43	41
MSD+L	9	25	12	88	51	124	9	32	67
MSD+R	10	23	16	77	50	49	9	91	38
MSD+S	27	31	20	88	51	124	10	90	67
MSDH	43	23	20	79	52	43	12	20	54

#### 4.1.3. Results and discussions

The FAR of each method is reported in Table 4. We first notice that classical subspace-based methods (OSP, MSD) are more effective than full-pixel (CEM) and statistical (AMF and sACE) methods. Next, we can see that, out of nine targets, MSDH outperforms all other methods on five targets and performs equally well on two target. MSDH also achieves the minimal sum of FARs. Then, comparing MSDH with noise estimation methods MSD+L, MSD+R and MSD+S, we see that the latter methods are not effective in improving the performance of MSD. While this is partially due to the low noise level of the HyMap dataset, it also suggests that estimating the noise intensity at pixel level is more effective than estimating that at image level. Last, compared with MSD only, MSDH improves the performance on six targets and the sum of FARs gets reduced from 0.085 to 0.018.

Moreover, to reduce the computational time, we apply the pre-screening method described in Sec. 3. We first apply MSD with  $r_b$  from 1 to 124, then select  $p = 2\%, 5\%, 10\%, \dots, 30\%$  of pixels that have the highest test statistics at each  $r_b$ , and finally apply MSDH on all these selected pixels. The performance of MSDH on the pre-screened dataset, denoted as MSDH- $p\%$ , is listed in Table 4 and Fig. 2a. When  $p = 2\%$ , the pixels that

Table 3: False Alarm Rates (FARs) for the HyMap dataset: ‘0’ indicates that the method does not generate any FA; ‘sum’ denotes the sum of FARs; the best results are in boldface.

	F1	F2	F3a	F3b	F4a	F4b	V1	V2	V3	sum
CEM	<b>0</b>	<b>0</b>	2.62e-02	7.61e-02	3.33e-05	4.18e-02	9.23e-02	7.47e-01	3.44e-02	1.02
AMF	<b>0</b>	<b>0</b>	3.77e-02	1.38e-01	3.33e-05	8.50e-02	1.85e-01	4.44e-01	5.80e-02	9.48e-01
sACE	<b>0</b>	<b>0</b>	3.36e-02	7.60e-02	<b>0</b>	8.88e-02	8.58e-02	7.73e-01	1.52e-02	1.07
OSP	<b>0</b>	<b>0</b>	1.90e-03	<b>4.97e-03</b>	<b>0</b>	3.83e-03	2.14e-02	4.27e-02	4.50e-03	7.93e-02
MSD	<b>0</b>	<b>0</b>	9.00e-04	1.10e-02	<b>0</b>	7.20e-03	1.46e-02	4.54e-02	5.93e-03	8.50e-02
MSD+L	<b>0</b>	<b>0</b>	4.50e-03	1.23e-02	<b>0</b>	2.67e-04	3.92e-02	4.66e-02	8.43e-03	1.11e-01
MSD+R	<b>0</b>	<b>0</b>	4.07e-03	1.88e-02	<b>0</b>	5.63e-03	4.43e-02	3.85e-02	1.56e-02	1.27e-01
MSD+S	<b>0</b>	<b>0</b>	4.43e-03	1.63e-02	<b>0</b>	2.33e-04	5.34e-02	6.07e-02	1.51e-02	1.50e-01
MSDH	<b>0</b>	<b>0</b>	<b>6.67e-05</b>	9.53e-03	3.33e-05	<b>2.00e-04</b>	<b>1.73e-03</b>	<b>5.43e-03</b>	<b>1.30e-03</b>	<b>1.83e-02</b>

contain certain targets are not selected and the MSDH will not work in this case. When  $p = 5\%$ , the FAR even reduces for three targets compared with the plain MSDH (i.e. without pre-screening). The reason is that MSD is relatively effective and it helps pre-screen out some pixels that are unlikely to contain the target. When  $p$  further increases, the performance on target detection becomes more similar to the plain MSDH; detailed results are omitted due to the space limit. In the experiment, we select  $p = 10\%$ , a choice that saves the computational time and guarantees the performance of the MSDH. Another way to reduce the computational time is to use fewer iterations. Fig. 2b shows that the performance of MSDH-10% with different numbers of iterations; MSDH-10% is used instead of the plain MSDH for computational efficiency. While the sum of FARs fluctuates slightly when the iteration number is from one to four, they all perform better than the MSD. Using one iteration gives a relatively good performance and is used as the default setting in our experiments.

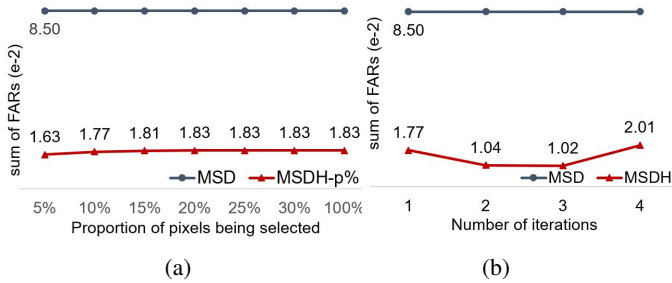


Fig. 2: HyMap dataset: (a) evaluation of the percentage of pre-screened pixels, i.e.  $p$ ; (b) evaluation of the number of iterations, i.e.  $M$ .

#### 4.1.4. Simulation study

The unknown type and magnitude of noise in the HyMap dataset may limit us from understanding the full capacity of MSDH. To confront with this problem, we carry out a simulation study where MSD and MSDH are evaluated on the dataset with more additive heterogeneous Gaussian noise added; this noise type satisfies the assumption of MSDH. The variance of the Gaussian white noise at band  $i$  is determined via the signal-

to-ratio (SNR), which is defined as

$$\text{SNR}_{\text{dB}} = 10 \log_{10} \frac{\sigma_{\text{image},i}^2}{\sigma_{\text{noise},i}^2}.$$

In our experiment, we calculate  $\sigma_{\text{image},i}^2$  from all pixels at band  $i$  and select  $\text{SNR} = 5$ , which gives the noise variance as  $\sigma_{\text{noise},i}^2 = 10^{-\frac{1}{2}} \sigma_{\text{image},i}^2$ . The plain MSDH is applied, i.e. using one iteration and without the pre-screening. Experiments are run for ten times and the performance in FAR (the lower the better) is summarised by using the boxplots in Fig. 3.

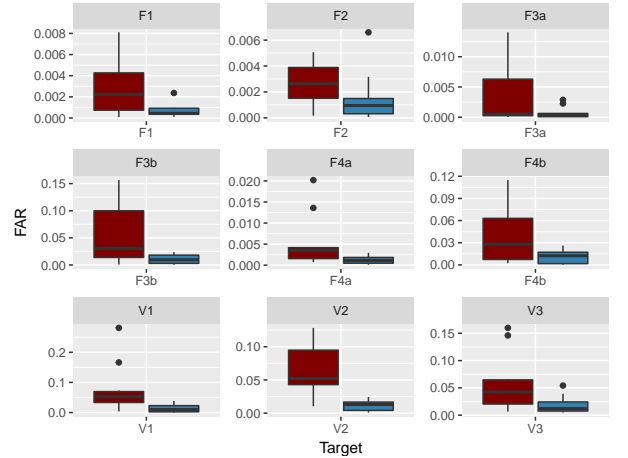


Fig. 3: FARs of MSD (left, in red) and MSDH (right, in blue) for the HyMap dataset with simulated heterogeneous Gaussian noise added. Lower FARs indicate the superiority of MSDH.

The MSDH reduces the mean and variance of FAR for all targets. This demonstrates that MSDH would be a more suitable method in the existence of heterogeneous noise.

## 4.2. The MUUFL Gulfport Collection

### 4.2.1. Data description

The MUUFL dataset was collected over the campus of the University of Southern Mississippi – Gulfport, located in Long Beach, Mississippi [43]. Three images are available and this experiment selects Gulfport Campus Flight 1. The image contains  $325 \times 337$  pixels with a spatial resolution of 1m and 72 spectral bands ranging from 367.7 to 1043.4 nm.

Table 4: Evaluation of pre-screening  $p$  percent of total pixels prior to MSDH. ‘NA’ indicates that none of the pre-selected pixels include the target.

FAR	F1	F2	F3a	F3b	F4a	F4b	V1	V2	V3	sum
2%	0	0	3.33e-05	5.97e-03	0	1.67e-04	1.67e-03	NA	9.67e-04	NA
5%	0	0	6.67e-05	8.40e-03	0	2.00e-04	1.73e-03	4.70e-03	1.20e-03	1.63e-02
10%	0	0	6.67e-05	9.17e-03	3.33e-05	2.00e-04	1.73e-03	5.23e-03	1.27e-03	1.77e-02

There were 64 targets of different colours, sizes, visibility and occlusion in the MUUFL collection. Targets were prepared in three sizes, namely  $0.5\text{m} \times 0.5\text{m}$ ,  $1\text{m} \times 1\text{m}$ , and  $3\text{m} \times 3\text{m}$ . By nature of MSD, our experiment only focuses on subpixel targets and hence targets of size  $0.5\text{m} \times 0.5\text{m}$  and  $1\text{m} \times 1\text{m}$  are chosen. In total, we have the following four types of targets: brown (BR, 10 samples), dark green (DG, 10 samples), pea green (PG, 10 samples), vineyard green and faux vineyard green (VG, 2 samples and FVG, 8 samples). Note that there is a mistake for vineyard green, where 1/5 of fabrics use the originally chosen fabric and the other 4/5 of the fabric was a different green [43]. The hyperspectral image and ground-truth target locations are shown in Fig. 4.

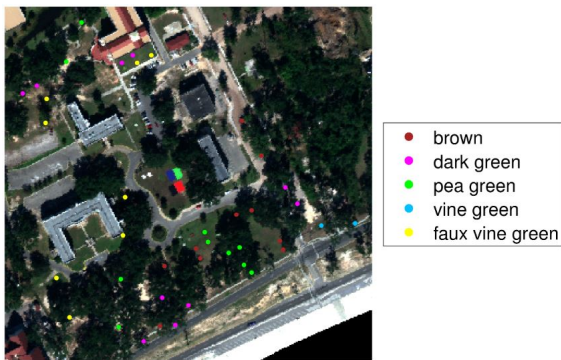


Fig. 4: The MUUFL Gulfport dataset in RGB and ground-truth locations of 40 targets in different colours.

#### 4.2.2. Experimental settings

For each subpixel target, a 5-by-5 square region around the ground-truth location defines its ROI so as to match the accuracy of the GPS device. When a subpixel target is being detected, pixels that locate in the ROI of the full-pixel target with the same type do not count into target nor false alarms; the ROI region is defined by a 7-by-7 square for full-pixel targets. All pixels which do not belong to the specified type are treated as the negative class. Since multiple samples are available for each type of target, we could calculate the false alarm rate and the detection power as the threshold  $\eta$  varies and it would be more informative to use the area under the receiver operating characteristic curve (AUC) statistic as the evaluation measure than a single FAR. The maximal detection score in each ROI is recorded as the score of positive class. A larger value of AUC suggests a better detection performance.

The background and target subspaces are constructed by using the same procedure as the HyMap dataset. For faux vineyard green, the library spectrum of vineyard green is used. The number of eigenvectors  $r_b$  is selected from the range of [1, 70] and the optimal value for each target is listed in Table 5.

Table 5: Parameter  $r_b$  in OSP, MSD and MSDH for the MUUFL dataset.

	BR	DG	PG	VG	FVG
OSP	39	38	58	11	22
MSD	23	38	40	27	22
MSD+L	48	38	43	12	38
MSD+R	39	39	42	70	36
MSD+S	39	34	42	10	22
MSDH	7	10	64	33	58

#### 4.2.3. Results and discussions

The AUC of each method is listed in Table 6. Once again, subspace-based methods show their effectiveness in subpixel target detection over full-pixel and statistical methods. The MSDH outperforms all other methods on three targets and achieves the highest average AUC. By using MSDH instead of MSD, the performance on four targets gets improved and the average of AUCs increases from 0.988 to 0.989.

Table 6: Area Under the Receiver Operating Characteristic Curve (AUCs) for the MUUFL dataset: ‘avg’ denotes the average of AUCs; the best results are in boldface.

	BR	DG	PG	VG	FVG	avg
CEM	0.960	0.957	0.963	0.977	0.938	0.959
AMF	0.964	0.969	0.971	0.982	0.929	0.963
sACE	0.982	0.954	0.950	0.955	0.940	0.956
OSP	<b>0.992</b>	0.981	0.974	0.996	0.971	0.983
MSD	0.991	0.985	0.982	0.996	0.985	0.988
MSD+L	0.975	<b>0.987</b>	0.977	0.994	0.976	0.982
MSD+R	0.981	0.973	0.974	0.990	0.963	0.976
MSD+S	0.984	0.971	0.971	0.991	0.962	0.976
MSDH	0.988	0.987	<b>0.984</b>	<b>0.998</b>	<b>0.987</b>	<b>0.989</b>

The pre-screening method is also applied to the MUUFL dataset. As shown in Fig. 5a, MSDH-5% performs worse than the MSD since pixels that contain some targets are not selected, MSDH-10% maintains the superiority of the MSDH, and MSDH-15%, ..., 30% behaves more similarly to the plain MSDH. The pattern is consistent with that observed for the HyMap dataset. Moreover, we evaluate the effect of using more iterations on MSDH-10% and observe substantial increase in the average AUC from Fig. 5b.

#### 4.2.4. Simulation study

We apply the same simulation setting as the HyMap dataset and add an independent multivariate Gaussian noise with an SNR of 5 at each band to the MUUFL dataset. Boxplots of AUC (the higher the better) of MSD and MSDH are shown in Fig. 6. The MSDH achieves higher mean and median AUC and lower variance than the MSD on all targets except VG. The

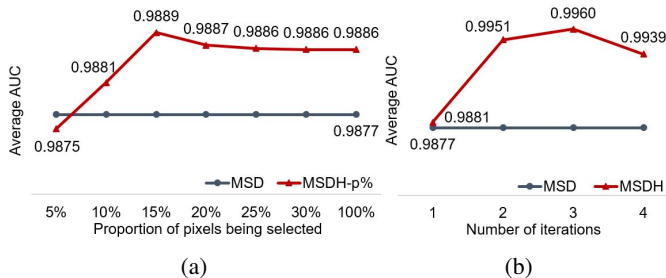


Fig. 5: MUUFL dataset: (a) evaluation of  $p$ ; (b) evaluation of  $M$ .

result again suggests that MSDH is promising in handling heterogeneous noise.

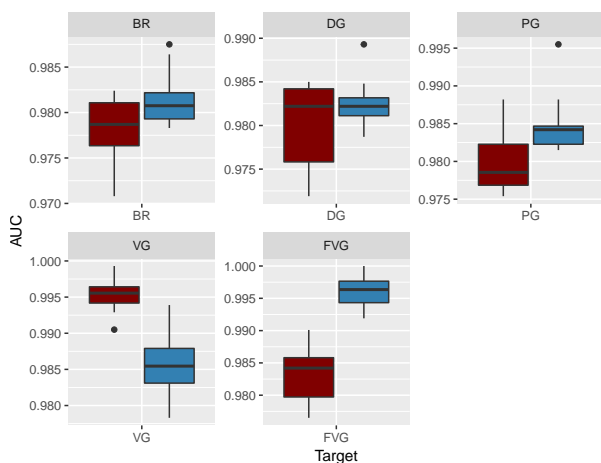


Fig. 6: AUCs of MSD (left, in red) and MSDH (right, in blue) for the MUUFL dataset with simulated heterogeneous Gaussian noise. Higher AUCs indicate the superiority of MSDH.

## 5. Conclusions and future work

This letter is aimed to introduce heterogeneous noise with unequal intensities over different bands to MSD, a classical subspace-based target detection method. We relaxed the noise assumption of MSD from equal variances to unequal ones and proposed a new target detection method termed MSDH. Experiments and simulation studies on the HyMap and MUUFL datasets show that MSDH gives a performance boost over MSD, highlighting the importance of modelling heterogeneous noise. The MSDH improves target detection performance at a cost of computational time. To reduce this side effect, we proposed a simple pre-screening method using MSD. Other fast and effective target detection methods could also be applied.

This work suggests the potential of addressing heterogeneous noise in HSI target detection through directly modelling the noise in the detector. Further investigation of spectrally-correlated noise and non-Gaussian noise is our future work.

## Acknowledgment

This work was partly supported by the Royal Society under Royal Society-Newton Mobility Grant IE161194, and by

the National Natural Science Foundation of China under Grant 61711530239.

## References

- [1] D. Manolakis, D. Marden, G. A. Shaw, Hyperspectral image processing for automatic target detection applications, *Lincoln Laboratory Journal* 14 (1) (2003) 79–116.
- [2] J. C. Harsanyi, C.-I. Chang, Hyperspectral image classification and dimensionality reduction: An orthogonal subspace projection approach, *IEEE Transactions on Geoscience and Remote Sensing* 32 (4) (1994) 779–785.
- [3] D. Manolakis, C. Siracusa, G. Shaw, Adaptive matched subspace detectors for hyperspectral imaging applications, in: *IEEE International Conference on Acoustics, Speech, and Signal Processing*, Vol. 5, IEEE, 2001, pp. 3153–3156.
- [4] E. J. Kelly, An adaptive detection algorithm, *IEEE Transactions on Aerospace and Electronic Systems* AES-22 (1) (1986) 115–127.
- [5] F. C. Robey, D. R. Fuhrmann, E. J. Kelly, R. Nitzberg, A CFAR adaptive matched filter detector, *IEEE Transactions on Aerospace & Electronic Systems* 28 (1) (1992) 208–216.
- [6] J. Broadwater, R. Chellappa, Hybrid detectors for subpixel targets, *IEEE Transactions on Pattern Analysis and Machine Intelligence* 29 (11) (2007) 1891–1903.
- [7] R. Li, S. Latifi, Improving hyperspectral subpixel target detection using hybrid detection space, *Journal of Applied Remote Sensing* 12 (1) (2018) 1–22.
- [8] H. Kwon, N. M. Nasrabadi, Kernel matched subspace detectors for hyperspectral target detection, *IEEE Transactions on Pattern Analysis and Machine Intelligence* 28 (2) (2006) 178–194.
- [9] Z. Wang, R. Zhu, K. Fukui, J.-H. Xue, Matched shrunken cone detector (MSCD): Bayesian derivations and case studies for hyperspectral target detection, *IEEE Transactions on Image Processing* 26 (11) (2017) 5447–5461.
- [10] Z. Wang, J.-H. Xue, The matched subspace detector with interaction effects, *Pattern Recognition* 68 (2017) 24–37.
- [11] Z. Wang, J.-H. Xue, Matched shrunken subspace detectors for hyperspectral target detection, *Neurocomputing* 272 (2018) 226–236.
- [12] H. Kwon, N. M. Nasrabadi, Kernel spectral matched filter for hyperspectral imagery, *International Journal of Computer Vision* 71 (2) (2007) 127–141.
- [13] Y. Chen, N. M. Nasrabadi, T. D. Tran, Sparse representation for target detection in hyperspectral imagery, *IEEE Journal of Selected Topics in Signal Processing* 5 (3) (2011) 629–640.
- [14] Y. Zhang, B. Du, L. Zhang, A sparse representation-based binary hypothesis model for target detection in hyperspectral images, *IEEE Transactions on Geoscience and Remote Sensing* 53 (3) (2015) 1346–1354.
- [15] B. Du, Y. Zhang, L. Zhang, D. Tao, Beyond the sparsity-based target detector: A hybrid sparsity and statistics-based detector for hyperspectral images, *IEEE Transactions on Image Processing* 25 (11) (2016) 5345–5357.
- [16] Y. Dong, B. Du, L. Zhang, Target detection based on random forest metric learning, *IEEE Journal of Selected Topics in Applied Earth Observations and Remote Sensing* 8 (4) (2015) 1830–1838.
- [17] J. Lu, J. Hu, Y.-P. Tan, Discriminative deep metric learning for face and kinship verification, *IEEE Transactions on Image Processing* 26 (9) (2017) 4269–4282.
- [18] J. Hu, J. Lu, Y.-P. Tan, Sharable and individual multi-view metric learning, *IEEE Transactions on Pattern Analysis and Machine Intelligence* 40 (9) (2017) 2281–2288.
- [19] A. Zare, C. Jiao, T. Glenn, Discriminative multiple instance hyperspectral target characterization, *IEEE Transactions on Pattern Analysis and Machine Intelligence* 40 (10) (2018) 2342–2354.
- [20] Y. Zhang, K. Wu, B. Du, X. Hu, Multitask learning-based reliability analysis for hyperspectral target detection, *IEEE Journal of Selected Topics in Applied Earth Observations and Remote Sensing*.
- [21] B. Rasti, P. Scheunders, P. Ghamisi, G. Licciardi, J. Chanussot, Noise reduction in hyperspectral imagery: Overview and application, *Remote Sensing* 10 (3) (2018) 482.
- [22] L. Gao, Q. Du, B. Zhang, W. Yang, Y. Wu, A comparative study on linear regression-based noise estimation for hyperspectral imagery, *IEEE Jour-*

- nal of Selected Topics in Applied Earth Observations and Remote Sensing 6 (2) (2013) 488–498.
- [23] M. O. Smith, P. E. Johnson, J. B. Adams, Quantitative determination of mineral types and abundances from reflectance spectra using principal components analysis, *Journal of Geophysical Research: Solid Earth* 90 (S02) (1985) C797–C804.
- [24] B. Thai, G. Healey, Invariant subpixel target identification in hyperspectral imagery, in: *Algorithms for multispectral and hyperspectral imagery V*, Vol. 3717, International Society for Optics and Photonics, 1999, pp. 14–25.
- [25] J. J. Faraway, *Linear Models with R*, Chapman and Hall/CRC, 2016.
- [26] S. Zhang, H. Zhou, F. Jiang, X. Li, Robust visual tracking using structurally random projection and weighted least squares, *IEEE Transactions on Circuits and Systems for Video Technology* 25 (11) (2015) 1749–1760.
- [27] N. Beyler, W. Fuller, S. Nusser, G. Welk, Predicting objective physical activity from self-report surveys: a model validation study using estimated generalized least-squares regression, *Journal of Applied Statistics* 42 (3) (2015) 555–565.
- [28] C. Shalizi, CMU 36-401 Modern Regression Section B Lecture Notes: Weighted and Generalized Least Squares, URL: <http://www.stat.cmu.edu/~cshalizi/mreg/15/>. Last visited on 01/Feb/2018 (2015).
- [29] L. Zhang, L. Zhang, D. Tao, X. Huang, B. Du, Hyperspectral remote sensing image subpixel target detection based on supervised metric learning, *IEEE Transactions on Geoscience and Remote Sensing* 52 (8) (2014) 4955–4965.
- [30] Y. Zhang, B. Du, L. Zhang, S. Wang, A low-rank and sparse matrix decomposition-based Mahalanobis distance method for hyperspectral anomaly detection, *IEEE Transactions on Geoscience and Remote Sensing* 54 (3) (2016) 1376–1389.
- [31] B. Du, L. Zhang, Target detection based on a dynamic subspace, *Pattern Recognition* 47 (1) (2014) 344–358.
- [32] A. Cloninger, W. Czaja, T. Doster, The pre-image problem for Laplacian eigenmaps utilizing  $l_1$  regularization with applications to data fusion, *Inverse Problems* 33 (7) (2017) 074006.
- [33] Y. Zhou, A. Rangarajan, P. D. Gader, A Gaussian mixture model representation of endmember variability in hyperspectral unmixing, *IEEE Transactions on Image Processing* 27 (5) (2018) 2242–2256.
- [34] S. Ozkan, B. Kaya, G. B. Akar, EndNet: Sparse autoencoder network for endmember extraction and hyperspectral unmixing, *IEEE Transactions on Geoscience and Remote Sensing* 57 (1) (2018) 482–496.
- [35] D. Snyder, J. Kerekes, I. Fairweather, R. Crabtree, J. Shive, S. Hager, Development of a web-based application to evaluate target finding algorithms, in: *IEEE International Geoscience and Remote Sensing Symposium*, Vol. 2, IEEE, 2008, pp. II–915.
- [36] W. Li, Q. Du, Collaborative representation for hyperspectral anomaly detection, *IEEE Transactions on Geoscience and Remote Sensing* 53 (3) (2015) 1463–1474.
- [37] A. P. Cisz, J. R. Schott, Performance comparison of hyperspectral target detection algorithms in altitude varying scenes, in: *Algorithms and Technologies for Multispectral, Hyperspectral, and Ultraspectral Imagery XI*, Vol. 5806, International Society for Optics and Photonics, 2005, pp. 839–849.
- [38] C.-I. Chang, D. C. Heinz, Constrained subpixel target detection for remotely sensed imagery, *IEEE Transactions on Geoscience and Remote Sensing* 38 (3) (2000) 1144–1159.
- [39] Y. Cohen, D. G. Blumberg, S. R. Rotman, Subpixel hyperspectral target detection using local spectral and spatial information, *Journal of Applied Remote Sensing* 6 (1) (2012) 1–16.
- [40] B.-C. Gao, An operational method for estimating signal to noise ratios from data acquired with imaging spectrometers, *Remote sensing of environment* 43 (1) (1993) 23–33.
- [41] J. M. Bioucas-Dias, J. M. Nascimento, Hyperspectral subspace identification, *IEEE Transactions on Geoscience and Remote Sensing* 46 (8) (2008) 2435–2445.
- [42] R. Roger, J. Arnold, Reliably estimating the noise in aviris hyperspectral images, *International Journal of Remote Sensing* 17 (10) (1996) 1951–1962.
- [43] P. Gader, A. Zare, R. Close, J. Aitken, G. Tuell, MUUFL Gulfport hyperspectral and LiDAR airborne data set, Tech. Rep. Rep. REP-2013-570, University of Florida, Gainesville, FL (Oct. 2013).